

Multiscale reweighted stochastic embedding (MRSE): Deep learning of collective variables for enhanced sampling

Jakub Rydzewski¹ and Omar Valsson²

¹⁾*Institute of Physics, Nicolaus Copernicus University, Grudziadzka 5, 87-100 Torun, Poland^{a)}*

²⁾*Max Planck Institute for Polymer Research, Ackermannweg 10, D-55128 Mainz, Germany^{b)}*

Machine learning methods provide a general framework for automatically finding and representing the essential characteristics of simulation data. This task is particularly crucial in enhanced sampling simulations, where we seek a few generalized degrees of freedom, referred to as collective variables (CVs), to represent and drive the sampling of the free energy landscape. These CVs should separate the different metastable states and correspond to the slow degrees of freedom. For this task, we propose a new method that we call multiscale reweighted stochastic embedding (MRSE). The technique automatically finds CVs by learning a low-dimensional embedding of the high-dimensional feature space to the latent space via a deep neural network. Our work builds upon the popular t -distributed stochastic neighbor embedding approach. We introduce several new aspects to stochastic neighbor embedding algorithms that makes MRSE especially suitable for enhanced sampling simulations: (1) a well-tempered selection scheme for the landmark features that gives close to equilibrium representation of the training data; (2) a multiscale representation via Gaussian mixture to model the probabilities of being neighbors in the high-dimensional feature space; and (3) a reweighting procedure to account for the training data being drawn from a biased probability distribution. To test the performance of MRSE, we use it to obtain low-dimensional CVs for two model systems, the Müller-Brown potential and alanine dipeptide, and provide a thorough analysis of the results.

Keywords: [Enhanced sampling](#) | [Collective variables](#) | [Machine learning](#) | [Dimensionality reduction](#) | [Parametric embedding](#)

I. INTRODUCTION

Modeling the long-timescale behavior of complex dynamical systems that vary over a wide range of spatial and temporal scales is a fundamental task in physical sciences. Molecular dynamics (MD) simulations allow us to probe the spatiotemporal details of molecular processes, but the so-called sampling problem severely limits their usefulness. This sampling problem comes from the fact that a typical free energy landscape is characterized by many metastable states separated by free energy barriers that are much higher than the thermal energy. Therefore, on the timescale one can simulate, barrier crossings are rare events, and the system remains kinetically trapped in a single metastable state. One way to solve this sampling problem is to employ enhanced sampling methods.¹ In particular, one class of such methods works by identifying a few critical slow degrees of freedom, commonly referred to as collective variables (CVs), and then enhancing their fluctuations by introducing an external bias potential.^{1–3}

The performance of CV-based enhanced sampling methods depends heavily on the quality of the CVs. Effective CVs should discriminate between the relevant metastable states and include most of the slow degrees of freedom.⁴ Typically, the CVs are constructed manually by using physical and chemical intuition, and there is a large selection of generally applicable CVs^{5–7} that have been developed and are available in open-source codes.^{5,8,9} However, despite immense progress in devising CVs, it may be far from trivial to construct a set of CVs that quantify all the essential characteristics of a system.¹⁰

^{a)}Electronic mail: jr@fizyka.umk.pl; ORCID: <https://orcid.org/0000-0003-4325-4177>

^{b)}Electronic mail: valsson@mpip-mainz.mpg.de; ORCID: <https://orcid.org/0000-0001-7971-4767>

Machine learning (ML) techniques provide an alternative solution to this problem by finding or constructing the CVs directly from the simulation data.^{11–14} Such dimensionality reduction methods typically work in a high-dimensional feature space (e.g., set of distances or dihedral angles) instead of directly using the microscopic coordinates, as this is much more efficient. They employ linear (e.g., principal component analysis,¹⁵ time-lagged independent component analysis¹⁶) or nonlinear (e.g., diffusion map,^{17–20} stochastic neighbor embedding (SNE),^{21–23} sketchmap,²⁴ UMAP²⁵) transformations. In the recent years, there has been a growing interest in performing dimensionality reduction with deep neural networks (NNs) to advance the field even further. Such methods, unlike the classical dimensionality reduction methods,^{26,27} provide embeddings that are parametric. Several interesting developments in application of NNs to MD simulations include variational autoencoders,^{28–31} time-lagged autoencoders,^{32,33} Gaussian mixture variational autoencoders,³⁴ variational approaches to Markov processes,^{35,36} generative models,^{37–41} deep linear discriminant analysis,⁴² and stochastic kinetic embedding.⁴³

In this work, we propose a proof-of-concept of our novel technique called multiscale reweighted stochastic embedding (MRSE) that unifies dimensionality reduction via deep NNs with enhanced sampling methods. The method constructs CVs by learning an NN embedding from a high-dimensional feature space to a low-dimensional latent space. Our work builds upon the promising and popular t -distributed SNE (t -SNE).^{22,23,44} We introduce several new aspects to SNE algorithms that makes MRSE particularly suitable for enhanced sampling simulations: (1) a well-tempered selection scheme for the landmark features that gives close to an equilibrium representation of the training data; (2) a multiscale representation via Gaussian mixture to model the probabilities in the high-dimensional feature space; and (3) a reweighting procedure to account for the training data being drawn from a biased probability distribution. We show a simplified outline of the protocol employed in this work in Fig. 1.

We note that our ultimate objective is to employ our MRSE method within an enhanced sampling scheme, where we will iteratively improve the CVs. However, in this work, we focus on the learning procedure. Therefore, to eliminate the influence of incomplete sampling, we employ idealistic sampling conditions that are generally not achievable in practice.⁴⁵ To gauge the performance of the learning procedure and the quality of the resulting embeddings, we apply MRSE to two model systems, the Müller-Brown potential and alanine dipeptide, and provide a thorough analysis of the results.

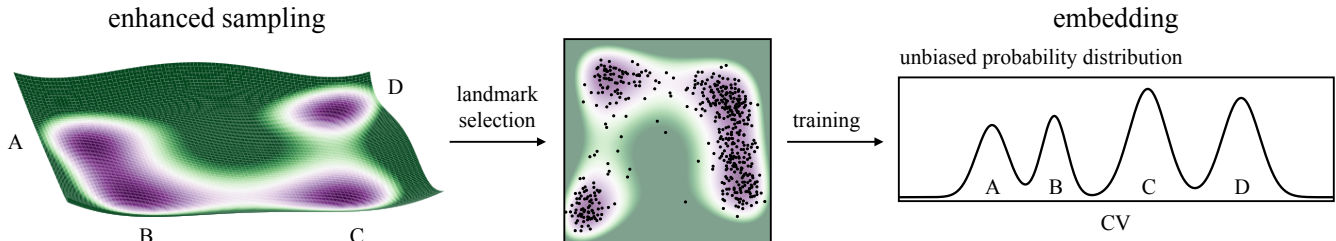


FIG. 1. Outline of the protocol introduced in this work. Our framework consists of (1) an enhanced sampling method that gives us features sampled from a biased probability distribution that we use as training data; (2) a landmark selection procedure that selects landmarks based on their statistical weights; and (3) a deep NN that learns low-dimensional CVs embedded in the latent space by minimizing a loss function.

II. METHODS

A. Collective variable based enhanced sampling

We start by giving a theoretical background on CV-based enhanced sampling methods. We consider a molecular system, described by microscopic coordinates \mathbf{R} and a potential energy function $U(\mathbf{R})$, which we want to study using MD or Monte Carlo simulations. Without loss of generality, we limit our discussion to the canonical ensemble (NVT).

At equilibrium, the microscopic coordinates follow the Boltzmann distribution:

$$P(\mathbf{R}) = \frac{e^{-\beta U(\mathbf{R})}}{\int d\mathbf{R} e^{-\beta U(\mathbf{R})}}, \quad (1)$$

where $\beta = (k_B T)^{-1}$ is the inverse of the thermal energy.

In CV-based enhanced sampling methods, we identify a small set of coarse-grained order parameters \mathbf{s} , generally referred to as CVs, that correspond to the essential slow degrees of freedom. The CVs are defined as $\mathbf{s}(\mathbf{R}) = [s_1(\mathbf{R}), s_2(\mathbf{R}), \dots, s_d(\mathbf{R})]$, where d is the number of CVs, and the dependence on \mathbf{R} can be either explicit or implicit, see below. Having defined the CVs, we obtain their equilibrium distribution as:

$$\begin{aligned} P(\mathbf{s}) &= \int d\mathbf{R} \delta[\mathbf{s} - \mathbf{s}(\mathbf{R})] P(\mathbf{R}) \\ &= \langle \delta[\mathbf{s} - \mathbf{s}(\mathbf{R})] \rangle, \end{aligned} \quad (2)$$

while the free energy surface (FES) is given by $F(\mathbf{s}) = -\beta^{-1} \log P(\mathbf{s})$.

In systems plagued by sampling problems, the FES is characterized by many metastable states separated by free energy barriers much larger than the thermal energy $k_B T$. Therefore, on the timescales we can simulate, the system stays kinetically trapped and is unable to explore the full FES. In other words, barrier crossings are rare events.

CV-based enhanced sampling methods overcome the sampling problem by introducing an external bias potential $V(\mathbf{s}(\mathbf{R}))$ acting in CV space that facilitates better sampling. We can trace this idea to the seminal work by Torrie and Valleau published in 1977.⁴⁶ Most of such methods adaptively construct the bias potential during the simulation to reduce free energy barriers or even completely flatten them. At convergence, the CVs then follow a biased distribution:

$$P_V(\mathbf{s}) = \frac{e^{-\beta[F(\mathbf{s})+V(\mathbf{s})]}}{\int d\mathbf{s} e^{-\beta[F(\mathbf{s})+V(\mathbf{s})]}} \quad (3)$$

that is easier to sample. CV-based methods differ in how they construct the bias potential and which kind of biased CV sampling they obtain at convergence. A non-exhaustive list of such techniques includes local elevation,⁴⁷ adaptive biasing force,⁴⁸ the Wang-Landau algorithm,⁴⁹ energy landscape paving,⁵⁰ Gaussian-mixture umbrella sampling,⁵¹ metadynamics,^{1,52,53} variationally enhanced sampling,^{54,55} and on-the-fly probability-enhanced sampling.⁵⁶

We focus here on well-tempered metadynamics (WT-MetaD)^{1,53} as this is the method we use in this work. However, we note that we can employ our MRSE technique with any CV-based enhanced sampling approach. For instance, another choice might be variationally enhanced sampling.

In WT-MetaD, the bias potential is constructed by periodically depositing repulsive Gaussian kernels at the current location in CV space. The height of the Gaussian is scaled according to a specific rule such that in the long-time limit the height goes to zero. At convergence, this leads to a so-called well-tempered distribution:

$$P_V(\mathbf{s}) = \frac{P(\mathbf{s})^{1/\gamma}}{\int d\mathbf{s} P(\mathbf{s})^{1/\gamma}}, \quad (4)$$

where γ is a positive parameter greater than 1, called bias factor, that determines how much we enhance CV fluctuations. The limit $\gamma \rightarrow 1$ corresponds to the unbiased ensemble, while the limit $\gamma \rightarrow \infty$ corresponds to conventional (non-well-tempered) metadynamics.⁵² If we take the logarithm on both sides of this equation, we can see that sampling the well-tempered distribution is equivalent to sampling an effective FES where the barriers of the original FES are reduced by a factor of γ . In general, one should select a bias factor γ such that effective free energy barriers become on the order of the thermal energy $k_B T$.

Next, we want to describe certain aspects of CV-based enhanced sampling methods as they are important for the discussion below.

Due to the external bias, each configuration \mathbf{R} carries an additional weight $w(\mathbf{R})$ that needs to be taken into account when calculating equilibrium properties. For a static bias potential, it is given by $w(\mathbf{R}) = e^{\beta V(\mathbf{s}(\mathbf{R}))}$. In WT-MetaD, we need to take into account the time-dependence of the bias potential. The weight is given by:

$$w(\mathbf{R}, t) = e^{\beta[V(\mathbf{s}(\mathbf{R})) - c(t)]}, \quad (5)$$

where $c(t)$ is a time-dependent constant that can be calculated from the bias potential at time t as:^{1,57}

$$c(t) = \frac{1}{\beta} \log \frac{\int d\mathbf{s} \exp \left[\frac{\gamma}{\gamma-1} \beta V(\mathbf{s}, t) \right]}{\int d\mathbf{s} \exp \left[\frac{1}{\gamma-1} \beta V(\mathbf{s}, t) \right]}. \quad (6)$$

There are also other ways for obtaining weights for reweighting WT-MetaD simulations.^{58–61}

In MD simulations, we do not only need to know the values of the CVs but also their derivatives w.r.t. the microscopic coordinates $\nabla_{\mathbf{R}} \mathbf{s}(\mathbf{R})$, as we need this to calculate the biasing force:

$$-\nabla_{\mathbf{R}} V(\mathbf{s}(\mathbf{R})) = -\partial_{\mathbf{s}} V(\mathbf{s}) \cdot \nabla_{\mathbf{R}} \mathbf{s}(\mathbf{R}). \quad (7)$$

In practice, however, the CVs might not depend directly on \mathbf{R} , but rather indirectly through another set of features or CVs $\mathbf{x}(\mathbf{R}) = [x_1(\mathbf{R}), x_2(\mathbf{R}), \dots, x_k(\mathbf{R})]$ of dimension k that depends on \mathbf{R} . In such cases, it is sufficient to know the derivatives of the CVs w.r.t. the input features, as we can obtain the total derivatives via the chain rule. In programs^{5,8,9} implementing CVs and enhanced sampling methods, like PLUMED^{8,62} that we use in this work, the code automatically takes care of applying the chain rule. Thus, when programming a CV, we only need to calculate the values and the derivatives w.r.t. to the input features $\mathbf{x}(\mathbf{R})$. In practice, we can even define a chain of multiple CVs that depend sequentially on each other.

Having provided the basics of CV-based enhanced sampling simulations, we now introduce our MRSE method for learning CVs.

B. Multiscale reweighted stochastic embedding (MRSE)

As a starting point for our method, we use t -SNE,²² a popular dimensionality reduction method that is derived from SNE.²¹ t -SNE has been used to analyze unbiased MD trajectories.^{63–66} We introduce here a parametric and multiscale variant of a SNE method aimed at learning CVs for atomistic simulations. In particular, we focus on using the method within enhanced sampling simulations, where we need to consider biased simulation data. We refer to this method as multiscale reweighted stochastic embedding (MRSE).

Consider a set of N observations of features $[\mathbf{x}_1, \dots, \mathbf{x}_N]^T$, each of dimension k , which we collect from a molecular simulation to be our training data. The features can be, for example, distances or dihedral angles. We use a parametric embedding function $f_{\theta}(\mathbf{x}) = \mathbf{s}(\mathbf{x})$ to map the high-dimensional feature space to the low-dimensional CV space (i.e., the latent space) $\mathbf{s} = [s_1, \dots, s_d]$, where d is the dimension of \mathbf{s} . Using these definitions, the problem of finding a low-dimensional set of CVs boils down to using the training data to find an optimal parametrization of θ for the embedding function using a non-linear ML model. We can then use the embedding as CVs and project any point in feature space to CV space.

1. Kullback-Leibler divergence as loss function

SNE methods approach dimensionality reduction by introducing pairwise probability distributions $P(\mathbf{x}_i, \mathbf{x}_j) \equiv p_{ij}$ and $Q(\mathbf{s}_i, \mathbf{s}_j) \equiv q_{ij}$ for distances in the feature and the latent space, respectively. The pairwise probability distributions are defined below in Sec. II B 2 and Sec. II B 4. The statistical distance between the two distributions is then minimized by introducing a loss function. Here, we use the Kullback-Leibler (KL) divergence (or the relative entropy^{67,68}) as a loss function. For this, we split the training data into B batches of size N_b . The KL divergence of one batch is then defined as:⁶⁹

$$D_{\text{KL}}(P\|Q) = \frac{1}{N_b} \sum_{i=1}^{N_b} \sum_{\substack{j=1 \\ i \neq j}}^{N_b} p_{ij} \log \left(\frac{p_{ij}}{q_{ij}} \right), \quad (8)$$

where $D_{\text{KL}}(\mathbf{P}||\mathbf{Q}) \geq 0$ with equality only when $\mathbf{P} = \mathbf{Q}$. For the probability matrix $\mathbf{P}(\mathbf{Q})$, the interpretation of a single element p_{ij} (q_{ij}) is that higher the value, higher is the probability of picking a feature \mathbf{x}_j (\mathbf{s}_j) as a neighbor of \mathbf{x}_i (\mathbf{s}_i). We show the derivation of the KL divergence for the full set of N training data in Appendix A1.

2. Feature pairwise probability distribution

We use kernel functions to describe the high-dimensional feature probability distribution.⁷⁰ We model the feature pairwise probability distribution as a discrete Gaussian mixture where each term is a Gaussian kernel, $K_{\epsilon_i}(\mathbf{x}_i, \mathbf{x}_j) = \exp(-\epsilon_i \|\mathbf{x}_i - \mathbf{x}_j\|_2^2)$ that is characterized by its bandwidth ϵ_i . As $\epsilon_i \neq \epsilon_j$, the kernels are not symmetric. We employ a Euclidean distance between data points $\|\cdot\|_2$, as is appropriate for representing high-dimensional data on a low-dimensional manifold.⁷¹ Then, a pair \mathbf{x}_i and \mathbf{x}_j that is embedded as two nearby points in the latent space has a higher probability of being neighbors than a pair that is embedded as two distant points.⁷² For a schematic representation of this, we refer to Fig. 2(a).

In the case of training data from an enhanced sampling simulation, we need to account for the fact that we are sampling the features from a biased probability distribution. Each feature \mathbf{x} then has an associated statistical weight $w(\mathbf{x})$. In this work, we primarily accomplish this task through the selection of the features used for the training by employing a selection scheme that takes the weights into account and gives close to an equilibrium representation of the training data, as described in Sec. II C. However, it is still beneficial to incorporate a reweighting procedure into the training as the selected features might have varying weights.

To account for the weights in the training of the embeddings, we follow Coifman²⁰ and define a reweighted Gaussian kernel as:

$$\tilde{K}_{\epsilon_i}(\mathbf{x}_i, \mathbf{x}_j) = r(\mathbf{x}_i, \mathbf{x}_j) K_{\epsilon_i}(\mathbf{x}_i, \mathbf{x}_j), \quad (9)$$

where $r(\mathbf{x}_i, \mathbf{x}_j) = \sqrt{w(\mathbf{x}_i)w(\mathbf{x}_j)}$ is a reweighting factor. The exact expression for the weights depends on the enhanced sampling method used. For example, in WT-MetaD simulations, the weights are given by Eq. 5. It might also be possible to use unbiased simulations at a higher temperature to train an embedding for a lower temperature. The weights would then account for the difference in temperature. If we collect the training data from a unbiased simulation, all the weights are equal to 1. We note that a similar symmetric weight $\sqrt{w(\mathbf{x}_i)w(\mathbf{x}_j)}$ is also used in Refs. 73 and 74.

A reweighted probability distribution for the feature space is then written as:

$$p_{ij}^{\epsilon} = \frac{\tilde{K}_{\epsilon_i}(\mathbf{x}_i, \mathbf{x}_j)}{\sum_k \tilde{K}_{\epsilon_i}(\mathbf{x}_i, \mathbf{x}_k)}, \quad (10)$$

where each p_{ij}^{ϵ} represents the pairwise probability of features \mathbf{x}_i and \mathbf{x}_j for a given set of bandwidths $\epsilon = [\epsilon_1, \epsilon_2, \dots, \epsilon_N]$, and $p_{ii}^{\epsilon} = 0$. The pairwise probabilities p_{ij}^{ϵ} are not symmetric due to the asymmetric kernels. This is in contrast to t -SNE, where the symmetry of the pairwise probabilities is enforced.²²

As suggested in the seminal work of Hinton and Roweis,²¹ the feature probability distribution can be extended to mixtures. To introduce such a multiscale procedure, we write the total probability distribution p_{ij} used in Eq. 8 as an average over different sets of bandwidths (i.e., a Gaussian mixture), as described in the following Sec. II B 3.

3. Multiscale representation

The bandwidths used for the Gaussian kernels in Eq. 10 are positive scaling factors that need to be optimized to estimate the density of the data. We can write $\epsilon_i = \frac{1}{2\sigma_i^2}$, where σ_i is the standard deviation of the kernel (Fig. 2(a)). We want a smaller σ_i in dense regions, and a larger σ_i in sparse regions. To achieve this task, we define the Shannon entropy of the i th Gaussian probability as:

$$H(\mathbf{x}_i) = - \sum_j p_{ij}^{\epsilon_i} \log p_{ij}^{\epsilon_i}, \quad (11)$$

where we note that $p_{ij}^{\epsilon_i}$ refers to the i th row of p_{ij}^ϵ as Eq. 11 is solved for each row of p_{ij}^ϵ independently.

Inserting $p_{ij}^{\epsilon_i}$ from Eq. 10 leads to the following expression:

$$H(\mathbf{x}_i) = \frac{1}{\tilde{p}_i} \left(\epsilon_i \sum_j p_{ij}^{\epsilon_i} \|\mathbf{x}_i - \mathbf{x}_j\|_2^2 - \underbrace{\sum_j p_{ij}^{\epsilon_i} \log r(\mathbf{x}_i, \mathbf{x}_j)}_{H_V(\mathbf{x}_i)} \right) + \log \tilde{p}_i, \quad (12)$$

where the factor $\tilde{p}_i = \sum_j p_{ij}^{\epsilon_i}$ is a row-wise normalization constant. The correction term $H_V(\mathbf{x}_i)$ is due to weights introduced in Eq. 10. If the weights are of exponential form, $w(\mathbf{x}_i) = e^{\beta V_i}$, like in WT-MetaD (Eq. 5, V_i then also includes the $c(t)$ factor), the reweighting factor is defined as $r(\mathbf{x}_i, \mathbf{x}_j) = \sqrt{e^{\beta V_i} e^{\beta V_j}}$, and the correction term takes a simpler form:

$$H_V(\mathbf{x}_i) = -\frac{\beta}{2} \left(V_i + \frac{1}{\tilde{p}_i} \sum_j p_{ij}^{\epsilon_i} V_j \right). \quad (13)$$

For the derivation of Eq. 12 and Eq. 13, see A2 in Appendix.

We use Eq. 12 to define an objective function for an optimization procedure that fits the Gaussian kernels to the data:

$$\min_{\epsilon_i} \left(H(\mathbf{x}_i) - \log_2 P \right), \quad (14)$$

where P is a model parameter that represents the perplexity of a discrete probability distribution. Perplexity is defined as an exponential of the Shannon entropy, $P = 2^H$, and measures the quality of predictions for a probability distribution.⁷⁵ We can view the perplexity as the effective number of neighbors in a manifold.^{22,23} To fit an optimal value of bandwidth, we perform the optimization procedure using a binary search for each row of the data.

For a given value of the perplexity P , we find the optimal set of bandwidth ϵ^P using Eqs. 12 and 14. We do this for multiple values of the perplexity, $P_l = 2^{L-l+1}$, where l goes from 0 to $L = \lfloor \log(N_b) \rfloor$. We then write the probabilities p_{ij} as an average over the different set of bandwidths:

$$p_{ij} = \frac{1}{N_P} \sum_P^{N_P} p_{ij}^{\epsilon^P}. \quad (15)$$

Therefore, by taking p_{ij} as a Gaussian mixture over different perplexities, we obtain a multiscale stochastic representation of the features.

In t -SNE, the perplexity is a fixed model parameter that the user needs to set. Thus, it is often customary to run multiple t -SNE embeddings for different perplexities to obtain an embedding with quantifiable characteristics.⁷⁶ Consequently, we can see that this multiscale representation of MRSE is of great advantage as we remove a single fixed perplexity value from the ML model. Furthermore, we do not need to select any perplexity parameters, and we obtain a parameter-free dimensionality reduction method. We note that our multiscale representation is similar to the one used in the multiscale SNE method presented in Ref. 77.

Having established the model of the pairwise probability distributions for the feature space, we now consider the latent space.

4. Latent pairwise probability distribution

A known issue, caused partly by the curse of dimensionality, which occurs in many dimensionality reduction methods is the so-called ‘‘crowding problem’’.^{21,78} In the context of atomistic simulation data, this issue leads to the definition of CVs that do not properly discriminate between metastable states, partially due to the use of highly-localized kernel

functions in the latent space. As can be seen in Fig. 2(b), if we change from a Gaussian kernel to a more heavy-tailed kernel, like a t -distribution kernel, we ensure that similar data points are grouped together and dissimilar data points are separated in the latent space.

For the pairwise probability distribution in the latent space, we use a heavy-tailed t -distribution, which is the same choice as in t -SNE. As discussed in Sec. IIB 1, we set $Q(\mathbf{s}_i, \mathbf{s}_j) \equiv q_{ij}$, which further translates to:

$$q_{ij} = \frac{\left(1 + \frac{1}{p} \|\mathbf{s}_i - \mathbf{s}_j\|_2^2\right)^{-\frac{p+1}{2}}}{\sum_k \left(1 + \frac{1}{p} \|\mathbf{s}_i - \mathbf{s}_k\|_2^2\right)^{-\frac{p+1}{2}}}, \quad (16)$$

where p represents the number of degrees of freedom of the t -distribution, and the latent variables (i.e., CVs) are obtained via the embedding function, e.g., $\mathbf{s}_i = f_{\boldsymbol{\theta}}(\mathbf{x}_i)$. As given in Ref. 23, we set $p = d - 1$, where d is the dimension of the latent space. In Eq. 16, $q_{ii} = 0$.

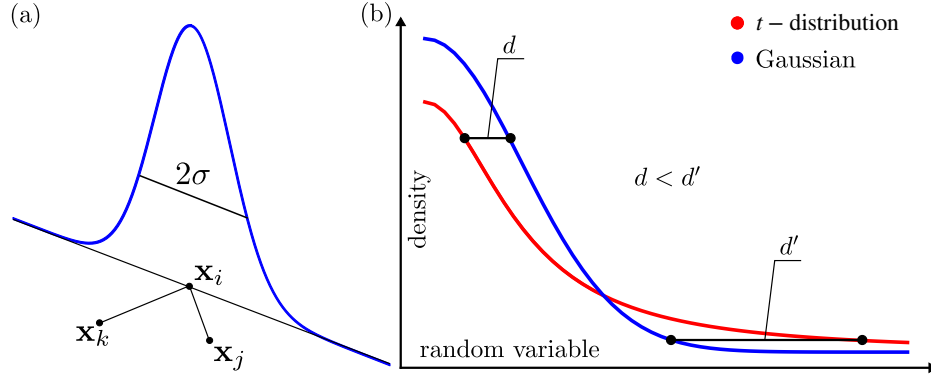


FIG. 2. Schematic representation depicting how MRSE (and also t -SNE) preserves the local structure of high-dimensional data. The probability matrices are represented by Gaussian kernels in the high-dimensional feature space and by the t -distribution kernels in the low-dimensional latent space. (a) The probability of picking the j th neighbor given the i th high-dimensional data point is modeled by a Gaussian kernel $\exp(-\epsilon_i \|\mathbf{x}_i - \mathbf{x}_j\|_2^2)$, where $\epsilon_i = 1/2\sigma^2$. (b) The minimization of the Kullback-Leibler divergence between the discrete probability distributions groups similar data points and separate dissimilar data points in the latent space. As the difference between the distributions fulfills $d' > d$, MRSE is likely to group similar points into metastable states that are properly separated.

5. Neural network embedding function

For the embedding function $f_{\boldsymbol{\theta}}(\mathbf{x})$, we employ a deep NN. See Fig. 3 for a schematic representation. NNs with at least one hidden layer are universal function approximators, and NNs with multiple layers (i.e., deep NNs) can express strongly non-linear functions with few nodes per layer.⁷⁹ Using an n -layer NN, we start from the feature space and reduce the dimensionality of the data through a succession of continuous non-linear mappings f :

$$f_{\boldsymbol{\theta}}(\mathbf{x}) = (f_n \circ \dots \circ f_1)(\mathbf{x}), \quad (17)$$

where the mappings f depend on the parameters $\boldsymbol{\theta}$ (i.e., the weights and biases of the NN).

To find the optimal parameters $\boldsymbol{\theta}$ for the NN embedded function, we use the training data to minimize the loss function (Eq. 8) w.r.t. to $\boldsymbol{\theta}$. We obtain the derivatives of the NN and the loss function w.r.t. $\boldsymbol{\theta}$ using backpropagation. In this work, we use the Adam optimizer⁸⁰ for the minimization of the loss function. For additional information about the training procedure, see Sec. IIID.

Once we have obtained the optimal parameters, we can use the parametric embedding function to project any given point in feature space to the latent space without re-running the training procedure. Therefore, we can use the

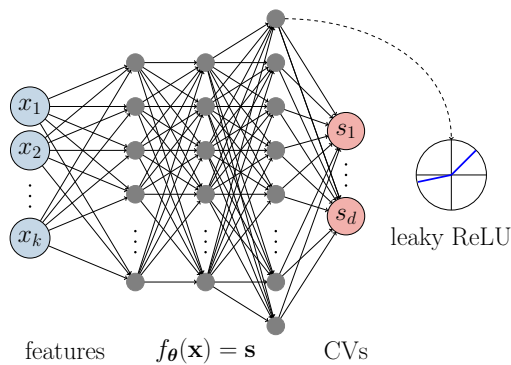


FIG. 3. Representation of the NN used to embed the high-dimensional feature space into a low-dimensional CV space (i.e., the latent space). The input features \mathbf{x} , $\dim(\mathbf{x}) = k$ are fed into the NN to generate the output CVs \mathbf{s} , $\dim(\mathbf{s}) = d$. In this schematic representation of the NN, the input layer is shown in blue, and the output layer is depicted in red. The hidden layers (gray) use dropout with a probability of 0.1, and the leaky ReLU activations. For more details, we refer to Sec. III C.

embedding (i.e., the NN) as CVs, $\mathbf{s}(\mathbf{x}) = f_{\theta}(\mathbf{x})$. We can obtain the derivatives of $f_{\theta}(\mathbf{x})$ w.r.t. \mathbf{x} using backpropagation. Using the chain rule, we can then calculate the derivatives of $\mathbf{s}(\mathbf{x})$ w.r.t. microscopic coordinates \mathbf{R} , which is needed to obtain the biasing force for enhanced sampling methods, as discussed in Sec. II A.

C. Well-tempered landmark selection

A critical point in getting accurate embeddings is the selection of the features in the training set. This is indeed an important issue in ML methods.^{81,82} The training set cannot be too large as the training procedure would take an excessively long time, and not too small as it would not represent all characteristics of the data. Instead, we need to select an appropriate number of landmark features (~ 1000) that best represent the underlying simulation data.^{83,84}

Ideally, we want the landmark features to be representative of the equilibrium distribution. In unbiased simulations, we can achieve this by selecting landmarks at random, or by collecting landmarks at some given frequency. In the case of biased simulations, however, we need to account for sampling from a biased distribution. One way to do this is the random sampling algorithm presented in Ref. 84, which takes the weights into account. However, as seen in Sec. IV B, by using such random sampling, we cannot get an equilibrium representation of metastable states lying higher in free energy, at least not for the test systems we employ here.

Another algorithm used for picking the landmarks is farthest point sampling (FPS).⁸⁵ The idea behind this is to select a set of landmark features from the initial simulation data that are most broadly spread. However, our experience for the systems tested here is that landmarks selected using FPS give bad embeddings, caused by the inclusion of features from higher-lying regions and the transition states.

In this work, we use a method called well-tempered farthest point sampling (WT-FPS).⁸⁶ This method allows interpolating between random selection and FPS. We give an intuitive explanation of how the procedure works below.

Assuming we want to select N landmarks from a simulation dataset that consists of M features, we start by selecting $K = \sqrt{NM}$ features using FPS. This is computationally inexpensive as compared to the full FPS. We then treat the K features as the centers of a Voronoi diagram that we build by assigning each of the $M - K$ remaining features to its nearest center. Next, we assign each center a weight obtained by summing over the weights of all the features that belong to it, $\omega(\mathbf{x}_i) = \sum_k w(\mathbf{x}_k)$. The Voronoi centers are uniformly spread, so we can define a measure of the density in the vicinity of center i as:

$$d_i = \frac{\omega(\mathbf{x}_i)}{\sum_{j=1}^K \omega(\mathbf{x}_j)}. \quad (18)$$

In the spirit of the well-tempered distribution⁵³ (Eq. 4), we introduce a parameter α and modify Eq. 18 as $\tilde{d}_i = d_i^{1/\alpha}$.

We proceed with selecting the remaining number of landmarks by selecting one of the centers at random, according to their weights \tilde{d}_i . We then choose at random one of the features belonging to that center, again taking the weights into account. We repeat this procedure until we have N landmarks.

If $\alpha = 1$, we recover the random sampling. However, by choosing $\alpha > 1$, we increasingly favor the algorithm to ignore the underlying probabilities, and pick a more uniformly distributed set of landmarks. In the limit of $\alpha \rightarrow \infty$, we obtain FPS. Thus, by using $\alpha > 1$ that is not too large, we can obtain a set of landmarks that better represent higher-lying metastable states while still not being too far from the equilibrium distribution, which is our objective when selecting landmarks from enhanced sampling simulations.

As the optimal value of α is case-dependent, we cannot say too much about what value to use in general. However, α should not be too large and ideally the smallest value that achieves a balanced selection. By balanced, we mean a landmark selection that is close to the equilibrium distribution and gives a proper representation of all metastable states but excludes points from higher-lying free energy regions and transition states.

D. Implementation

We implemented both the MRSE method and the WT-FPS landmark selection algorithm in an additional module in a development version (2.7.0-dev) of the open-source PLUMED^{8,62} enhanced sampling plug-in. We use the LibTorch⁸⁷ library (PyTorch C++ API, git commit 89d6e88) that allows us to perform immediate execution of dynamic tensor computations with automatic differentiation.⁸⁸

Having a PLUMED implementation of our MRSE method is of great benefit as we can use it with all the MD codes that PLUMED supports and learn CVs both in post-processing and on-the-fly during a simulation. Furthermore, PLUMED implements the calculation of various features/CVs that we can use as input features. We can then use the learned CVs in the different CV-based enhanced sampling methods implemented in PLUMED. We will make our code publicly available under open-source license by contributing the module to the official PLUMED repository in the near future.

III. COMPUTATIONAL DETAILS

A. Müller-Brown potential

We consider the dynamics of a single particle moving on the two-dimensional Müller-Brown potential:⁸⁹

$$U(x, y) = \alpha \sum_{j=0}^3 A_j \exp [a_j(x - x_{0,j})^2 + b_j(x - x_{0,j})(y - y_{0,j}) + c_j(y - y_{0,j})^2], \quad (19)$$

where x, y are the particle coordinates, and A, a, b, c, x_0 and y_0 are the parameters of the potential given by $A = (-200, -100, -170, 15)$, $a = (-1, -1, 6.5, 0.7)$, $b = (0, 0, 11, 0.6)$, $c = (-10, -10, -6.5, -0.7)$, $x_0 = (1, 0, -0.5, -1)$, and $y_0 = (0, 0.5, 1.5, 1)$. We can see the form of the potential in Fig. 4(a). We employ units such that $k_B = 1$ and write all values as unitless. We reduce the height of the highest barrier from around 120 to 20 by employing a scaling factor of $\alpha = 0.2$.

What matters for the dynamics of the particle is the ratio of the barrier height to the thermal energy $k_B T$. Here, we simulate the system at a temperature of $T = 1$, such that $k_B T = 1$. Therefore, we have a substantial barrier of around $20 k_B T$ between the two states and a rare event system. For the coordinates x and y , there is no CV projection needed, and we can obtain the reference FES directly from the potential, $F(x, y) = U(x, y)$.

For the WT-MetaD simulations, we use the `pesmd` code from the PLUMED enhanced sampling package.^{8,62} The `pesmd` code implements a simple MD integrator with a Langevin thermostat⁹⁰ for analytical model potentials. We employ a time step of 0.005 and a friction coefficient of 10 for the Langevin thermostat.

In the WT-MetaD simulations, we take x and y as CVs. We use the bias factors of 3, 5, 7, 10, and 20, and an initial Gaussian height of 1.2, a Gaussian width of 0.1 for both CVs, and deposit Gaussians every 200 steps. The simulations are run for a total time of 100000 ($2 \cdot 10^7$ steps). We calculate the $c(t)$ factor needed for the weights every time a Gaussian is added using Eq. 6 as implemented in PLUMED (using a grid of 500×500 over the domain $[-5, 5] \times [-5, 5]$).

When training the embeddings from the WT-MetaD simulations, we skip the first 20% of the runs (up to step $4 \cdot 10^6$) to ensure that we avoid the period at the beginning of the simulations where the weights might be unreliable due to rapid changes in the bias potential. To avoid numerical issues, we normalize the weights such that they lie in the range 0 to 1.

For the embeddings, we use the coordinates x and y as input features ($k = 2$), while the number of output CVs is also 2 ($d = 2$). We do not standardize or preprocess the input features.

B. Alanine dipeptide

We perform the alanine dipeptide (Ace-Ala-Nme) simulations using the GROMACS 2019.2 code⁹¹ patched with a development version of the PLUMED plug-in.^{8,62} We use the Amber99-SB force field,⁹² and a time step of 2 fs. We perform the simulations in the canonical ensemble at 300 K using the stochastic velocity rescaling thermostat⁹³ with a relaxation time of 0.1 fs. We constrain hydrogen bonds using LINCS.⁹⁴ We perform the simulations in vacuum where we employ no periodic boundary conditions and no cut-offs for the electrostatic and non-bonded van der Waals interactions.

For the parallel tempering (PT) simulation, we employ 4 replicas with temperatures distributed according to a geometrical distribution in the range of 300 K to 800 K (300.0 K, 416.0 K, 576.9 K, 800.0 K). We run the PT simulation for 100 ns per replica. We attempt exchanges between neighboring replicas every 10 ps. We obtain the FESs from the PT simulation using a histogram in which we use 300 bins for each CV. We use only the 300 K replica for analysis.

We perform the WT-MetaD simulations using the backbone dihedral angles Φ and Ψ as CVs and different values for the bias factor (2, 3, 5, 10, and 20), as discussed below. We use an initial Gaussian height of 1.2 kJ/mol, a Gaussian width of 0.2 rad for both CVs, and deposit Gaussians every 1.0 ps. We run the WT-MetaD simulations for 100 ns. We calculate the $c(t)$ factor needed for the weights every time a Gaussian is added using Eq. 6 as implemented in PLUMED (using a grid of 500×500 over the domain $[-\pi, \pi] \times [-\pi, \pi]$).

When training the embeddings from the WT-MetaD simulations, we skip the first 20 ns to ensure that we avoid the period at the beginning of the simulations where the weights might be unreliable due to rapid changes in the bias potential. To avoid numerical issues, we normalize the weights such that they lie in the range 0 to 1.

For the embeddings, we use 21 heavy atoms pairwise distances as input features ($k = 21$), while the number of output CVs is 2 ($d = 2$). To obtain an impartial selection of features, we start with all 45 heavy atoms pairwise distances. Then, to avoid unimportant features, we automatically check for low variance features and remove all distances with a variance smaller than $2 \cdot 10^{-4} \text{ nm}^2$ from the training set (see Fig. S2 in the SM). This procedure removes 24 distances, and we are left with 21 distances that we use for the embeddings (both training and projections). The remaining distances are standardized such that their mean is zero, and their standard deviation is 1.

We note that we only do this trimming of distances to avoid including redundant features into the NN that only add noise to the training procedure. There is no intrinsic limitation to MRSE that limits us to using this number of features.

C. Neural network architecture

For the NN architecture (size and number of layers), we use the same setup as from the work of van der Maaten and Hinton.^{23,95} Namely, the NN consists of an input layer with a size equal to the dimension of the feature space k , followed by three hidden layers of sizes $h_1 = 500$, $h_2 = 500$, and $h_3 = 2000$, and an output layer with a size equal to the dimension of the latent space d . For the MB potential and alanine dipeptide, we use k equal to 2 and 21, respectively. In both cases the embeddings map the feature space to 2D latent space ($d = 2$). For the details regarding the architecture of NNs, see Tab. I.

The following details differ from the NN setup used in Refs. 23 and 95. To allow for any output value, we do not wrap the output layer within an activation function. Moreover, for all hidden layers, we employ leaky rectified linear units (ReLU)⁹⁶ with a leaky parameter set to 0.2. Each hidden layer is followed by a dropout layer⁹⁷ (dropout probability $p = 0.1$) as dropping out nodes with a small probability value reduces overfitting. The dropout layer is only used during the training.

We note that we tried to reduce the number of nodes in each of the NN layers, but this resulted in a bad embedding that was unable to discriminate between the metastable states. We find the NN architecture used here to work well for the systems examined in this study, although modifications may be needed when considering more complex and challenging cases.

D. Training procedure and hyperparameters

We use the WT-FPS algorithm to select 2000 landmark features that we use as training data. Unless otherwise indicated, we use $\alpha = 5$ for the selection (see Eq. 18). We then shuffle the selected landmark features and divide them into batches of size 500. We initialize all trainable weights of the NNs with the Glorot normal scheme⁹⁸ using the gain value calculated for leaky ReLU. The bias parameters of the NNs are initialized with 0.005.

We minimize the KL divergence between feature probability distribution and latent probability distribution using the Adam optimizer,⁸⁰ where we use learning rate $\eta = 10^{-3}$, and momenta $\beta_1 = 0.9$ and $\beta_2 = 0.999$. We also employ a standard L2 regularization term on the trainable network parameters θ in the form of weight decay set to 10^{-4} . We perform the training for 100 epochs in all cases. The KL divergence learning curves for the systems considered here are shown in Figs. S7 and S8 of the SM.

We report all hyperparameters used to obtain the results in this work in Tab. I. For reproducibility purposes, we also list the random seeds used while launching the training (the seed affects both the landmark selection and the shuffling of the landmark features during the training). The training procedure and hyperparameters used here worked well for the systems examined in this study, but modifications may be needed when analyzing more difficult cases.

TABLE I. Hyperparameters used to obtain the results reported in this paper.

Hyperparameter	Müller-Brown	Alanine dipeptide
Architecture	[2, 500, 500, 2000, 2]	[21, 500, 500, 2000, 2]
Optimizer	Adam	Adam
Number of samples	$N = 2000$	$N = 2000$
Batch size	$N_b = 500$	$N_b = 500$
Training iterations	100	100
Learning rate	10^{-3}	10^{-3}
Seed	111	111 (main text); 222, 333 (SM)
Leaky parameter	0.2	0.2
Dropout	0.1	0.1
Weight decay	10^{-4}	10^{-4}
β_1 and β_2	0.9 and 0.999	0.9 and 0.999

E. Cluster analysis

We perform the cluster analysis on the MRSE embeddings by fitting a Bayesian Gaussian mixture⁹⁹ to the data. We run this procedure with the number of components (clusters) equal to 4, where each component has its own general covariance matrix. We use the `scikit-learn` machine-learning library¹⁰⁰ and `scipy`¹⁰¹ to perform this analysis.

F. Data availability

We used git commit 89d6e88 of LibTorch to obtain all results. All the data and PLUMED input files required to replicate the results presented in the main text are available from the PLUMED Consortium repository⁶² under plumID:XX.YYY at <https://www.plumed-nest.org/eggs/XX/YYY/> (will be added upon publication).

IV. RESULTS

A. Müller-Brown potential

We start by considering a single particle moving on the two-dimensional Müller-Brown potential shown in Fig. 4. We use this system as a simple test to check if the MRSE method can preserve the topography of FES when performing a simple 2D to 2D mapping, in the absence of any dimensionality reduction. In other words, we select the dimensionalities of the feature space and the latent space to be equal. Such simple mappings are known to be a problem for some methods, e.g., variational autoencoders as shown in Figure 4(d) in Ref 34.

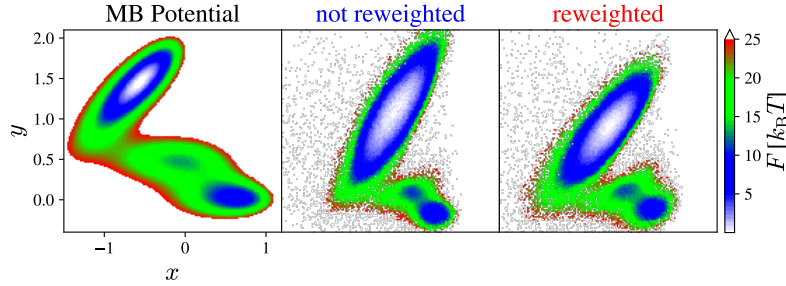


FIG. 4. MRSE embeddings for the Müller-Brown potential (1st panel) obtained from the WT-MetaD simulation with bias factor $\gamma = 5$. We show FESs for the embeddings obtained without (2nd panel) and with (3rd) incorporating weights during the training. The units for the MRSE embeddings are arbitrary and thus not shown.

We train the MRSE embeddings on biased simulation data coming from WT-MetaD simulations using the coordinates x and y as CVs. Here we show results obtained with $\gamma = 5$, while the results for the remaining bias factors (3, 7, 10, 20) are shown in Fig. S1 in the SM.

We present the FESs obtained with the MRSE embeddings in Fig. 4. We can see that the embeddings preserve the topography of the FESs well and demonstrate a fine separation of metastable states, both when we incorporate the weights into the training (see Eq. 9), and when we do not. The same can be said for most of the other bias factor shown in Fig. S1 in the SM.

In Fig. 5, we show how the embeddings map the x and y coordinates. We can see that most of the points lie along the identity line, which shows that the embeddings preserve well the original coordinates of the system. In other words,

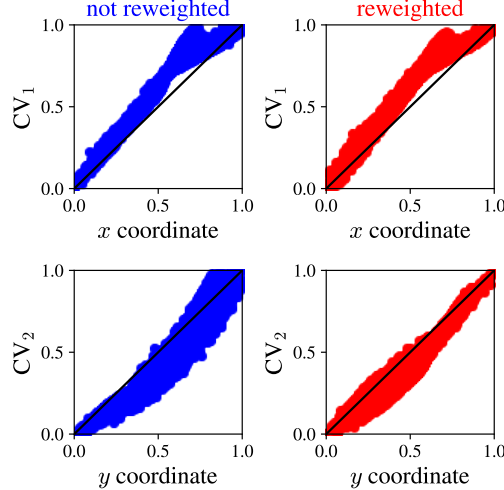


FIG. 5. Normalized Müller-Brown coordinates x and y versus the normalized CVs from the MRSE embedding. The MRSE embeddings for the Müller-Brown potential are obtained from the WT-MetaD simulation with bias factor $\gamma = 5$. We show how the embeddings map the coordinates x and y . We show both reweighted (red) and non-reweighted (blue) embeddings.

the embeddings maintain distances between points when going from the feature space to the latent space. We analyze this point in a detailed manner for a more high-dimensional system in Sec. IV B.

B. Alanine dipeptide

Next, we consider alanine dipeptide in vacuum, a small system often used to benchmark free energy and enhanced sampling methods. The free energy landscape of the system is described by the backbone (Φ, Ψ) dihedral angles as shown in Fig. 7(a), where we can see that the FES is characterized by three metastable states. We can consider the $C7_{eq}$ and $C5$ states as one superstate since these states are only separated by a small barrier of around $1-2 k_B T$, so transitions between the two states are frequent. The $C7_{ax}$ state lies higher in free energy (i.e., is less probable) and is separated by a high barrier of around $14 k_B T$ from the other two states. Generally, the (Φ, Ψ) angles are taken as CVs for biasing, though for this particular setup in vacuum it is sufficient to bias Φ to drive the sampling between states (i.e., Ψ is a fast CV compared to Φ).

In the training of the MRSE embeddings, we do not use the (Φ, Ψ) angles as input features, but rather a set of 21 heavy atom pairwise distances that we have impartially selected in an automated way as described in Sec. III B. Using only the pairwise distances as input features makes the exercise of learning CVs more challenging as the Φ and Ψ angles cannot be represented as linear combinations of the interatomic distances. We can assess the quality of our results by how well the MRSE embeddings preserve the topography of the FES. However, before considering the MRSE results, let us consider the landmark selection, which we find to be a rather crucial issue to get accurate embeddings.

As discussed in Sec. II C, we need to have a landmark selection scheme that takes into account the weights of the configurations and gives a balanced selection that ideally is close to the equilibrium distribution. Our choice is WT-FPS⁸⁶ that has a single parameter α that interpolates between random and FPS selection of landmarks. In Fig. 6, we show the results using the WT-FPS scheme for one of the WT-MetaD simulations ($\gamma = 5$).

For $\alpha = 1$, which is equivalent to a random selection with weights, we can see that we get an insufficient representation of the $C7_{ax}$ state. We can understand this by looking at the weights of configurations in the $C7_{ax}$ state as they are considerably smaller than the weights from the other states. As expected, using the $\alpha = 1$ landmark selection results in a poor MRSE embedding due to the lack of data from the $C7_{ax}$ state (see Fig. S5 in the SM).

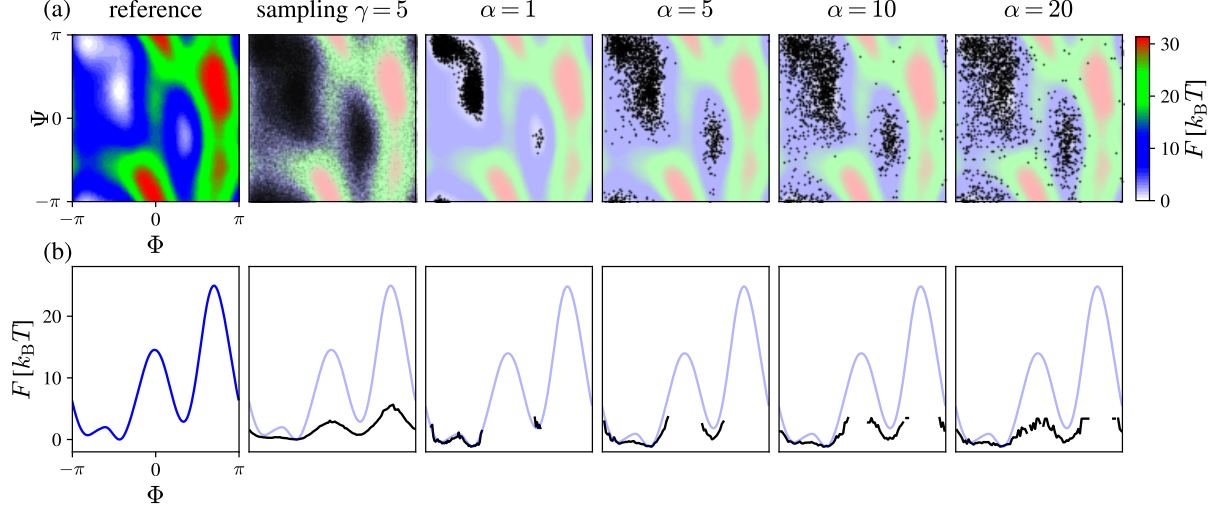


FIG. 6. Results of WT-FPS landmark selection for the WT-MetaD simulation ($\gamma = 5$) for alanine dipeptide biasing (Φ, Ψ). (a) In the first two panels, we show in the (Φ, Ψ) space, the reference FES and the points sampled during the simulations. In the subsequent panels, we show the 2000 landmarks selected for different values of the α parameter. (b) In the bottom row, we show the results projected on Φ , where the reference FES is shown in light blue. The projections (black) are calculated as a negative logarithm of the histogram of the selected landmarks.

However, we can see that using $\alpha = 5$ yields a much more balanced selection that is relatively close to the equilibrium distribution, as shown in the FES projected on Ψ in the bottom row in Fig. 6. Using larger values of α results in selections closer to the sampling from the underlying biased simulation, with more features higher in free energy. We observed that using $\alpha = 5$ gave the best results for the MRSE embeddings. In contrast, higher values of α resulted in embeddings characterized by the overlapping metastable states, as can be seen in Fig. S6 in the SM for the $\alpha = 20$ case. The reason for this worse behavior for higher values of α is the inclusion of features from higher-lying regions and the transition states in the training dataset. Therefore, in the following, we use WT-FPS with $\alpha = 5$ for the landmark selection.

The above results for WT-FPS landmark selection underline the importance of having a balanced selection of landmarks that is close to the equilibrium distribution and gives a proper representation of all metastable states but excludes points from higher-lying free energy regions and transition states. The exact value of α that achieves such optimal selection depends on the energy landscape of the system of interest. Though we cannot say too much about what value to use in general, it is clear that α should not be too large and ideally the smallest value that achieves a balanced selection.

Having established how to perform the landmark selection, we now consider result for MRSE embeddings trained on unbiased and biased simulation data. The unbiased simulation data comes from a parallel tempering (PT) simulation that gives an accurate description of the equilibrium distribution.¹⁰² We refer to the embedding trained on this data as the PT embedding. The biased simulation data comes from WT-MetaD simulations biasing the (Φ, Ψ) angles where we employ different values of the bias factor γ , going from 2 to 20. We refer to these embeddings as the WT-MetaD embeddings. Here we use the bias factor to generate a set of biased simulations that progressively go from a biased distribution closer to the equilibrium one to more flatter distribution as we increase γ (see Eq. 4). In this way, we can test how the MRSE reweighting procedure works when handling simulation data obtained under different biasing strengths. To be consistent and allow for a fair comparison, after training the embeddings, we always apply them to the same PT simulation data and use the resulting projections to perform all analysis and to generate the FESs.

In Fig. 7, we show the FESs obtained from the different MRSE embedding. In Fig. 8, we also show results of cluster analysis (see Sec. III E for the details) of the data that shows how the different embedding map the metastable states. Both the PT embedding in Fig. 7(b) and the WT-MetaD embeddings in the upper row of Fig. 7(c) are somewhat similar. We can see from Fig. 8 that the embeddings preserves the topography of the FES and correctly map the important metastable states from the feature space to the latent space. This means that the embeddings map both

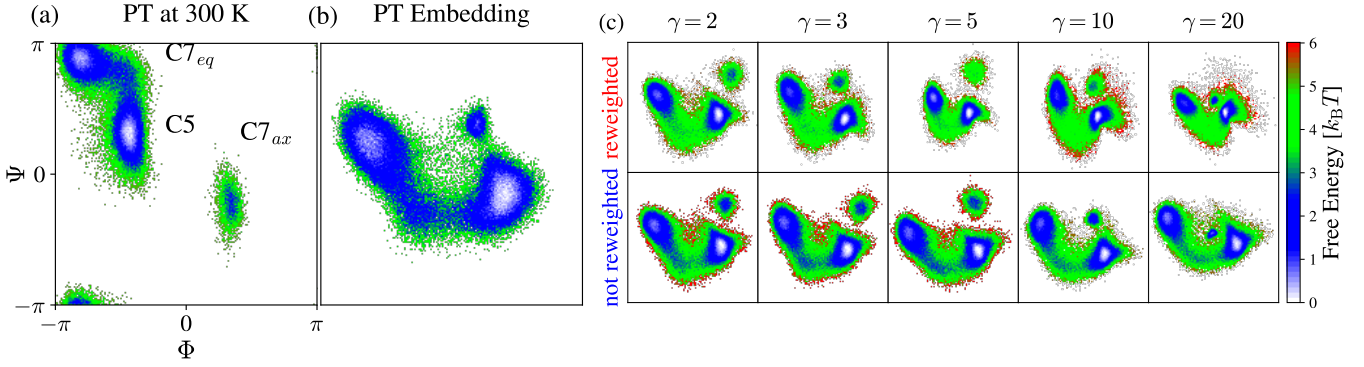


FIG. 7. Results of the MRSE embeddings on unbiased and biased simulation data of alanine dipeptide in vacuum at 300 K. (a) The free energy landscape $F(\Phi, \Psi)$ from the PT simulation. The metastable states $C7_{eq}$, $C5$, and $C7_{ax}$ are shown. (b) The FES for the MRSE embedding trained using the unbiased PT simulation data. (c) The FESs for the MRSE embeddings trained using WT-MetaD simulation data. We show results obtained from runs using different bias factors γ . The upper row (reweighted) shows results obtained by incorporating weights (see Eq. 9), while the lower row shows results obtained by not incorporating weights (not reweighted). We obtain all the FESs using the PT simulation data. The units for the MRSE embeddings are arbitrary and thus not shown.

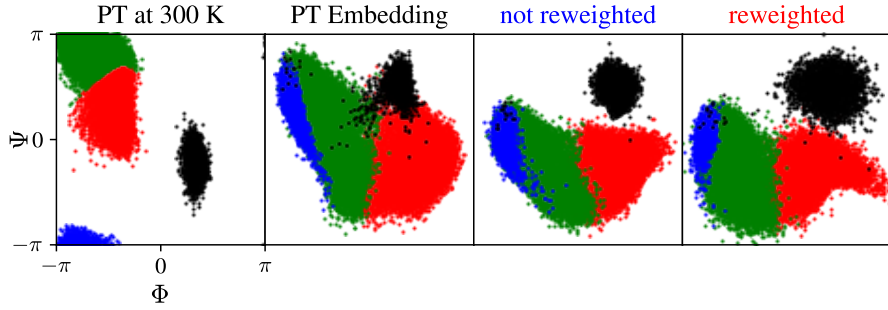


FIG. 8. Clustering of the data from the PT simulation at 300 K for the different embeddings (See Sec. III E). The results show how the embeddings map the metastable states. The clustered data points are colored accordingly to their cluster. The first panel shows the metastable state clusters in the (Φ, Ψ) space. The second panel shows the results for the PT embedding. The third and fourth panels show the results for the WT-MetaD embedding, using $\gamma = 5$ as a representative case, obtain without and with reweighting, respectively. We note that due to periodic boundary conditions, the $C7_{eq}$ metastable state is split into two separate clusters (blue and green). The units for the MRSE embeddings are arbitrary and thus not shown.

the local and global similarities accurately. For the WT-MetaD embeddings, we can see that the $\gamma = 20$ embedding is slightly worse than the others, but this can be explained by the high bias factor used, see below.

Next, we investigate the effect of not incorporating the weights into the training of the WT-MetaD embeddings (i.e., not using them in Eq. 9). We can see in the lower row of Fig. 7(c) that the embeddings are mostly similar to the reweighted ones in the upper panel. This similarity is most likely because the WT-FPS scheme already takes the weights into account. The $\gamma = 10$ and $\gamma = 20$ embeddings seem to be slightly better when not incorporating the weights.

To further check the quality of the embeddings, we calculate the free energy difference between the different metastable states:¹

$$\Delta F_{A,B} = -\frac{1}{\beta} \log \frac{\int_A ds e^{-\beta F(s)}}{\int_B ds e^{-\beta F(s)}}, \quad (20)$$

where the integration domains are the regions in CV space corresponding to the states A and B, respectively. This equation is only valid if the CVs correctly discriminate between the different metastable states. We can thus calculate the free energy differences for the different embeddings and compare them to a reference value. A deviation from the reference value indicates that the embedding does not correctly map the metastable states. In Fig. 9, we show the results for the free energy differences for the embeddings. The reference values are obtained by doing the integration

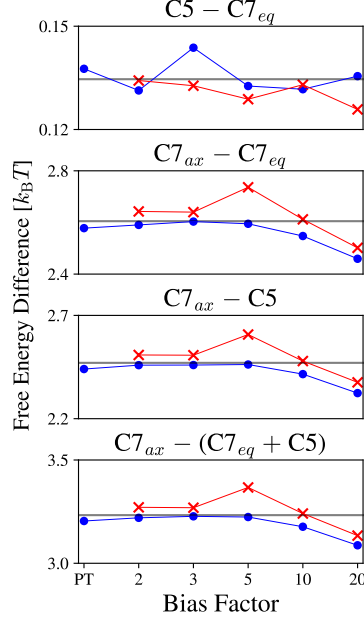


FIG. 9. Free energy differences between different metastable states of alanine dipeptide for the FESs obtained with the embeddings shown in Fig. 7. We show the reference values from the (Φ, Ψ) FES for the PT simulation as horizontal gray lines. The results for the reweighted embeddings are shown as blue dots, while the non-reweighted embeddings are shown as red dots.

in the (Φ, Ψ) FES for the PT simulation (Fig. 7). The results are consistent with our conclusions from Figs. 7 and 8, and corroborate the reliability of the embeddings. All free energy differences obtained with the MRSE embeddings agree with the reference values within a $0.5 k_B T$ uncertainty.

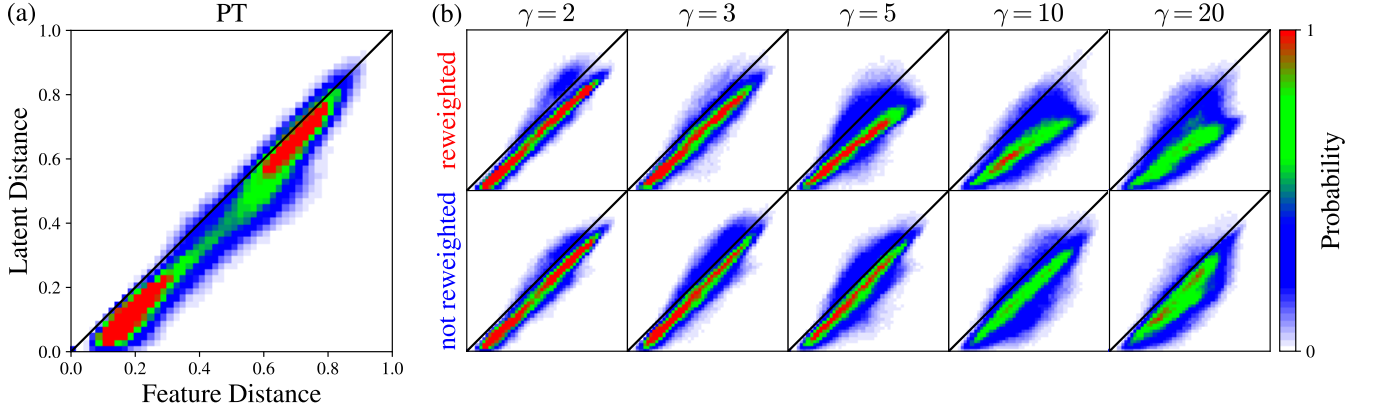


FIG. 10. The joint histogram of distances in the high-dimensional feature space and the low-dimensional latent space. We show the results for the embeddings shown in Fig. 7. We show the identity line $y = x$ as a black line. For an ideal embedding, all the density would lie on this line. We have normalized the distances to lie in the range 0 to 1.

As a final test of our embeddings, we follow the approach presented by Tribello and Gasparotto^{83,84} to compare different dimensionality reduction methods. We calculate distances between points in the high-dimensional feature space and the corresponding distances between points in the low-dimensional latent (i.e., CV) space given by the embeddings. We then calculate the joint histogram of the distances. The density will be concentrated on the identity line if an embedding is perfect. As we can see in Fig. 10, for most embeddings, the density is concentrated close to the identity line.

For the WT-MetaD embeddings with $\gamma > 3$, we can see for the reweighted embeddings that the density for middle distances is distributed non-linearly along the identity line, in contrast to the non-reweighted embeddings. This difference is due to using an additional criterion during the training of the embedding: apart from Euclidean distances, we also include the weights. However, we can expect this difference, as having points with low weights in the feature space will decrease the probability of being neighbors with these points in the latent space.

Looking at Figs. 7, 9, and 10 together, we can see that the $\gamma = 10$ and $\gamma = 20$ embeddings are worse than the embeddings with the lower bias factors. This worse behavior is very likely because the biased CV distribution has started to deviate much more from the equilibrium distribution in these simulations. Therefore, it is harder for the WT-FPS scheme to get good landmarks. And the reweighting during the training is unable to correct for this. However, we do not think this a significant issue. Bias factors $\gamma > 10$ are unnecessarily large for this particular system. It is sufficient to employ a bias factor of around 5 to get a good sampling. Therefore, when judging our results, we should focus on the WT-MetaD embeddings for the lower bias factors that are remarkably good.

To test the effect of the stochastic nature of the method, we obtain embeddings with two other predefined random seeds, see Figs. S3 and S4 in the SM. Apart from some irrelevant rotation, the embeddings are similar to ones shown in Fig. 7 on both local and global scales. We can see that from Fig. 7 and Figs. S3 and S4 that all embeddings obtained with the same random seed are rotated similarly, despite being trained on different simulation data. We believe this to be due to the initialization of the NN, which depends on the seed and thus is the same for all embeddings obtained with the same seed. In any case, a rotation of the embeddings is irrelevant. We can always apply a transformation to the embeddings to rotate them if needed.

V. DISCUSSION AND CONCLUSIONS

ML methods are quickly making an impact in the field of atomistic simulations. They provide a general framework for automatically finding and representing the essential characteristics of the simulation data. This task is particularly crucial in the field of enhanced sampling simulations. In CV-based enhanced sampling simulations, we seek a few generalized degrees of freedom (i.e., CVs) to represent and drive the sampling of the free energy landscape. The CVs should separate the different metastable states and correspond to all the slow degrees of freedom. For this task, we propose here a method called multiscale reweighted stochastic embedding (MRSE). This method can find CVs automatically by learning a low-dimensional embedding from a high-dimensional feature space.

The MRSE method is parametric as we employ a deep NN for the embedding function representing the CVs. Thus, once we have learned the embeddings, we can use the NN to project any given point in feature space to the CV space without re-running the training procedure. Furthermore, we can obtain the derivatives of the NN with respect to the input features, and therefore bias the learned CVs within enhanced sampling simulations. We will make use of this property in future work.

For the model system used in this work, we have used up to 21 input features for the MRSE embeddings. However, as we construct the probability matrices for the high-dimensional feature space through kernels,⁷⁰ the method scales well with the dimension of the feature space. Therefore, we can employ MRSE with a larger number of input features, compared to the number used in this work. In fact, *t*-SNE, which is the starting point for our method and also employs kernels for the feature space, has been used with up to 10^4 input features.²² Only when using larger feature spaces are we likely to need larger training datasets, but this is not an issue as we discuss in the following.

A significant limitation of SNE methods is the poor scalability of the probability matrices with the size of the dataset. Instead, in our approach, we feed the NNs in batches and compute the probability matrices only within each batch. That reduces the memory restrictions immensely and allows us to train MRSE embeddings on datasets of virtually any size. Additionally, as discussed in Ref. 23, parametric techniques using only an encoder network, like *t*-SNE and MRSE, provide computational advantages over autoencoders, which consists of an encoder part and a decoder part, during the training stage. As a result, in our MRSE method, derivatives (i.e., errors in ML terminology) have to be backpropagated through roughly half the number of NN layers as compared to autoencoders.

One of the issues with using kernel-based dimensionality reduction methods like diffusion maps²⁰ and SNE algorithms²¹ is that the user needs to select bandwidths for the Gaussian kernels. It is not always clear what values to use. For

example, in t -SNE,^{22,23} one optimizes a single Gaussian bandwidth to match a parameter called perplexity, which we can view as the effective number of neighbors. However, this only redirects the issue. Now the question is — how to select the perplexity value?⁷⁶ Larger perplexities lead to a larger number of nearest neighbors and to an embedding that is less sensitive to small topographic structures in the data. Conversely, a lower perplexity considers a smaller number of neighbors, and thus ignores more global information in favor of the local neighborhood. Furthermore, what if several length scales characterize the data? In this case, it is impossible to represent the density of the data with a single bandwidth. In t -SNE, it may be challenging to grasp the topological details within a single embedding. Instead, people resort to viewing multiple embeddings obtained with different perplexities.⁷⁶

In our MRSE method, we circumvent the issues of selecting the bandwidth or perplexity by employing a multiscale representation of the feature space, as described in Sec. II B 3. Instead of a single Gaussian kernel, we use a Gaussian mixture where each term has a bandwidth optimized for a different perplexity value. We perform this procedure in an automated way so that the user does not have to think about selecting any parameter. The multiscale representation allows us to describe both local and global characteristics of the underlying topography. This multiscale nature of MRSE makes the method particularly suitable for investigating complex systems, where the free energy landscape consists of several metastable states of different sizes.

Using ML methods is particularly tricky when considering training data obtained from enhanced sampling simulations. In this case, we sample the features from a biased probability distribution and need to consider a reweighting procedure to correct for this. In this work, we address this issue in a twofold way.

First, we use the WT-FPS landmark selection scheme that takes into account the weights of the configurations. This scheme allows us to obtain a balanced selection of landmarks that is close to the equilibrium distribution. Although MRSE does not require any parameters, the WT-FPS landmark selection scheme depends on the choice of the α parameter. The exact α value to be used is case-dependent. However, one should try to select it such that one obtains a landmark selection that gives a proper representation of all metastable states but excludes points from higher-lying free energy regions and transition states.

Second, we propose a reweighting scheme based loosely on the one used in diffusion maps.^{20,74} This scheme provides a way to incorporate weights into the training of the MRSE embeddings via reweighted Gaussian kernels. For the system considered in this work, the MRSE embeddings obtained by including the weights are slightly different, though it is hard for us to conclude that including the weights improves the embeddings, in fact, the opposite seems to be the case for some of the results. This is most likely because we already include the weights when selecting the landmarks with the WT-FPS scheme, which seems to be a more critical issue and mostly solves the reweighting problem. However, we should not take too much from these results as this might be a rather system-dependent issue. Therefore, we need to consider further the effect of reweighting on the MRSE embeddings in future work.

We implemented the MRSE method into the PLUMED enhanced sampling plug-in. This native PLUMED implementation has numerous benefits. We can use the MRSE method with the various MD codes that PLUMED support. We can use MRSE to learn CVs in post-processing, like we have done here, and on-the-fly during a simulation. We will make use of on-the-fly training in future work, as discussed below. PLUMED implements the calculation of various features/CVs that we can use as input features for MRSE embeddings. Finally, we can employ the learned CVs with the different biasing methods implemented in PLUMED. We will make MRSE publicly available by contributing the code to the official PLUMED repository in the near future.

In this work, we have focused on the learning procedure, when employing unbiased and biased simulation data, and the effect of reweighting. Therefore, to eliminate the influence of incomplete sampling, we have employed idealistic sampling conditions that are not always achievable in practice.⁴⁵ We can clearly observe the promising performance of the MRSE method for learning CVs from the results presented here. The next step is to use the MRSE method within an enhanced sampling scheme, where we will iteratively improve the CVs, in a similar fashion to other techniques.^{30,31,43,103,104} We will pursue this objective in future work.

ACKNOWLEDGEMENTS

We want to thank Ming Chen (UC Berkeley) and Gareth Tribello (Queen's University Belfast) for useful discussions, and Robinson Cortes-Huerto, Oleksandra Kukharenko, and Joseph F. Rudzinski (Max Planck Institute for Polymer Research) for carefully reading over the manuscript. JR gratefully acknowledges financial support by the Foundation for Polish Science (FNP). We acknowledge usage of the MPCDF (Max Planck Computing & Data Facility) DataShare.

APPENDIX

A1. KULLBACK-LEIBLER DIVERGENCE LOSS BETWEEN $P(\mathbf{x}_i, \mathbf{x}_j)$ AND $Q(\mathbf{s}_i, \mathbf{s}_j)$ FOR FULL SET OF TRAINING DATA

We present a derivation of the KL divergence between two pairwise probability distributions $P(\mathbf{x}_i, \mathbf{x}_j)$ and $Q(\mathbf{s}_i, \mathbf{s}_j)$ given by Eq. 8. For discrete probability distributions p and q defined on the same probability space χ , the KL divergence of p and q is defined to be:

$$D_{\text{KL}}(p \parallel q) = \sum_{x \in \chi} p(x) \log \left(\frac{p(x)}{q(x)} \right), \quad (\text{A1})$$

where $q(x) = 0$ implies $p(x) = 0$, and the base of the logarithm is arbitrary. For two pairwise probability matrices, Eq. A1 needs to be rewritten as the row-wise average of the KL divergences:⁶⁹

$$D_{\text{KL}}(P \parallel Q) = \frac{1}{N_b} \sum_{i=1}^{N_b} D_{\text{KL}}(P_i \parallel Q_i), \quad (\text{A2})$$

where P_i and Q_i are the i rows of $P(\mathbf{x}_i, \mathbf{x}_j)$ and $Q(\mathbf{s}_i, \mathbf{s}_j)$, respectively, and N_b is the number of rows in the matrices or the batch size. Then, if we take an average of the partial KL divergence losses for all B batches of the data using Eq. A2, we arrive at Eq. 8 for the full set of training data:

$$D_{\text{KL}}(P \parallel Q) = \frac{1}{B} \sum_{b=1}^B \frac{1}{N_b} \sum_{i=1}^{N_b} \sum_{\substack{j=1 \\ i \neq j}}^{N_b} p_{ij} \log \left(\frac{p_{ij}}{q_{ij}} \right) \quad (\text{A3})$$

$$= \frac{1}{N} \sum_{b=1}^B \sum_{i=1}^{N_b} \sum_{\substack{j=1 \\ i \neq j}}^{N_b} p_{ij} \log \left(\frac{p_{ij}}{q_{ij}} \right). \quad (\text{A4})$$

A2. SHANNON ENTROPY FOR THE REWEIGHTED GAUSSIAN KERNEL

Here we derive Eq. 12 and Eq. 13 from Sec. II B 3. The Shannon entropy of a discrete Gaussian kernel is:

$$H(\mathbf{x}_i) = - \sum_j p_{ij}^{\epsilon_i} \log p_{ij}^{\epsilon_i}, \quad (\text{A5})$$

where $p_{ij}^{\epsilon_i}$ is the i th row of the reweighted feature probability distribution:

$$p_{ij}^{\epsilon} = \frac{\tilde{K}_{\epsilon_i}(\mathbf{x}_i, \mathbf{x}_j)}{\sum_k \tilde{K}_{\epsilon_k}(\mathbf{x}_i, \mathbf{x}_k)}, \quad (\text{A6})$$

for the reweighted Gaussian kernel $\tilde{K}_{\epsilon_i}(\mathbf{x}_i, \mathbf{x}_j) = r(\mathbf{x}_i, \mathbf{x}_j)K_{\epsilon_i}(\mathbf{x}_i, \mathbf{x}_j)$, where $r(\mathbf{x}_i, \mathbf{x}_j)$ is a reweighting factor. We define a row-wise normalization constant of Eq. A6 as $\tilde{p}_i = \sum_k \tilde{K}_{\epsilon_i}(\mathbf{x}_i, \mathbf{x}_k)$. By plugging Eq. A6 to Eq. A5, we arrive at:

$$H(\mathbf{x}_i) = -\frac{1}{\tilde{p}_i} \sum_j \tilde{K}_{\epsilon_i}(\mathbf{x}_i, \mathbf{x}_j) \log \left(\frac{1}{\tilde{p}_i} \tilde{K}_{\epsilon_i}(\mathbf{x}_i, \mathbf{x}_j) \right) \quad (\text{A7})$$

$$= -\frac{1}{\tilde{p}_i} \sum_j \tilde{K}_{\epsilon_i}(\mathbf{x}_i, \mathbf{x}_j) \log \left(\frac{1}{\tilde{p}_i} r(\mathbf{x}_i, \mathbf{x}_j) K_{\epsilon_i}(\mathbf{x}_i, \mathbf{x}_j) \right) \quad (\text{A8})$$

$$= -\frac{1}{\tilde{p}_i} \sum_j \tilde{K}_{\epsilon_i}(\mathbf{x}_i, \mathbf{x}_j) \left(\log r(\mathbf{x}_i, \mathbf{x}_j) + \log K_{\epsilon_i}(\mathbf{x}_i, \mathbf{x}_j) - \log \tilde{p}_i \right) \quad (\text{A9})$$

$$= -\frac{1}{\tilde{p}_i} \sum_j \tilde{K}_{\epsilon_i}(\mathbf{x}_i, \mathbf{x}_j) \left(\log r(\mathbf{x}_i, \mathbf{x}_j) - \epsilon_i \|\mathbf{x}_i - \mathbf{x}_j\|_2^2 - \log \tilde{p}_i \right) \quad (\text{A10})$$

$$= \frac{1}{\tilde{p}_i} \left(\epsilon_i \sum_j \tilde{K}_{\epsilon_i}(\mathbf{x}_i, \mathbf{x}_j) \|\mathbf{x}_i - \mathbf{x}_j\|_2^2 - \sum_j \tilde{K}_{\epsilon_i}(\mathbf{x}_i, \mathbf{x}_j) \log r(\mathbf{x}_i, \mathbf{x}_j) + \underbrace{\log \tilde{p}_i \sum_j \tilde{K}_{\epsilon_i}(\mathbf{x}_i, \mathbf{x}_j)}_{=\tilde{p}_i} \right) \quad (\text{A11})$$

$$= \frac{1}{\tilde{p}_i} \left(\epsilon_i \sum_j \tilde{K}_{\epsilon_i}(\mathbf{x}_i, \mathbf{x}_j) \|\mathbf{x}_i - \mathbf{x}_j\|_2^2 - \sum_j \tilde{K}_{\epsilon_i}(\mathbf{x}_i, \mathbf{x}_j) \log r(\mathbf{x}_i, \mathbf{x}_j) \right) + \log \tilde{p}_i \quad (\text{A12})$$

$$= \frac{1}{\tilde{p}_i} \epsilon_i \sum_j \tilde{K}_{\epsilon_i}(\mathbf{x}_i, \mathbf{x}_j) \|\mathbf{x}_i - \mathbf{x}_j\|_2^2 - \frac{1}{\tilde{p}_i} \sum_j \tilde{K}_{\epsilon_i}(\mathbf{x}_i, \mathbf{x}_j) \log r(\mathbf{x}_i, \mathbf{x}_j) + \log \tilde{p}_i \quad (\text{A13})$$

$$= H_U(\mathbf{x}_i) + H_V(\mathbf{x}_i) + \log \tilde{p}_i. \quad (\text{A14})$$

The full Shannon entropy vector is $H = [H(\mathbf{x}_1), H(\mathbf{x}_2), \dots, H(\mathbf{x}_N)]^T$.

If the weights are given by WT-MetaD, then $H_V(\mathbf{x}_i)$ may be further reduced:

$$H_V(\mathbf{x}_i) = -\frac{1}{\tilde{p}_i} \sum_j \tilde{K}_{\epsilon_i}(\mathbf{x}_i, \mathbf{x}_j) \log r(\mathbf{x}_i, \mathbf{x}_j) \quad (\text{A15})$$

$$= -\frac{1}{\tilde{p}_i} \sum_j \tilde{K}_{\epsilon_i}(\mathbf{x}_i, \mathbf{x}_j) \log \sqrt{e^{\beta V_i} e^{\beta V_j}} \quad (\text{A16})$$

$$= -\frac{\beta}{2\tilde{p}_i} \sum_j \tilde{K}_{\epsilon_i}(\mathbf{x}_i, \mathbf{x}_j) (V_i + V_j) \quad (\text{A17})$$

$$= -\frac{\beta}{2} \left(\frac{1}{\tilde{p}_i} \sum_j \tilde{K}_{\epsilon_i}(\mathbf{x}_i, \mathbf{x}_j) V_j + V_i \right), \quad (\text{A18})$$

which is Eq. 13 from the main text.

- ¹ O. Valsson, P. Tiwary, and M. Parrinello, “Enhancing important fluctuations: Rare events and metadynamics from a conceptual viewpoint,” *Ann. Rev. Phys. Chem.* **67**, 159–184 (2016).
- ² Y. I. Yang, Q. Shao, J. Zhang, L. Yang, and Y. Q. Gao, “Enhanced sampling in molecular dynamics,” *J. Chem. Phys.* **151**, 070902 (2019).
- ³ G. Bussi and A. Laio, “Using metadynamics to explore complex free-energy landscapes,” *Nat. Rev. Phys.*, **1** (2020).
- ⁴ F. Noé and C. Clementi, “Collective variables for the study of long-time kinetics from molecular trajectories: Theory and methods,” *Curr. Opin. Struct. Biol.* **43**, 141–147 (2017).
- ⁵ G. Fiorin, M. L. Klein, and J. Hénin, “Using collective variables to drive molecular dynamics simulations,” *Mol. Phys.* **111**, 3345–3362 (2013).
- ⁶ C. Abrams and G. Bussi, “Enhanced sampling in molecular dynamics using metadynamics, replica-exchange, and temperature-acceleration,” *Entropy* **16**, 163–199 (2014).
- ⁷ F. Pietrucci, “Strategies for the exploration of free energy landscapes: Unity in diversity and challenges ahead,” *Reviews in Physics* **2**, 32–45 (2017).
- ⁸ G. A. Tribello, M. Bonomi, D. Branduardi, C. Camilloni, and G. Bussi, “PLUMED 2: New feathers for an old bird,” *Comp. Phys. Commun.* **185**, 604–613 (2014).
- ⁹ H. Sidky, Y. J. Colón, J. Helfferich, B. J. Sikora, C. Bezik, W. Chu, F. Giberti, A. Z. Guo, X. Jiang, J. Lequieu, and et al., “SSAGES: Software suite for advanced general ensemble simulations,” *The Journal of Chemical Physics* **148**, 044104 (2018).
- ¹⁰ I. G. Kevrekidis, C. W. Gear, J. M. Hyman, P. G. Kevrekidis, O. Runborg, and C. Theodoropoulos, “Equation-free, coarse-grained multiscale computation: Enabling microscopic simulators to perform system-level analysis,” *Commun. Math. Sci.* **1**, 715–762 (2003).
- ¹¹ P. Mehta, M. Bukov, C.-H. Wang, A. G. R. Day, C. Richardson, C. K. Fisher, and D. J. Schwab, “A high-bias, low-variance introduction to machine learning for physicists,” *Phys. Rep.* **810**, 1–124 (2019).
- ¹² Y. Wang, J. M. L. Ribeiro, and P. Tiwary, “Machine learning approaches for analyzing and enhancing molecular dynamics simulations,” *Curr. Opin. Struct. Biol.* **61**, 139–145 (2020).
- ¹³ F. Noé, A. Tkatchenko, K.-R. Müller, and C. Clementi, “Machine learning for molecular simulation,” *Ann. Rev. Phys. Chem.* **71**, 361–390 (2020).
- ¹⁴ G. Carleo, I. Cirac, K. Cranmer, L. Daudet, M. Schuld, N. Tishby, L. Vogt-Maranto, and L. Zdeborová, “Machine learning and the physical sciences,” *Rev. Mod. Phys.* **91**, 045002 (2019).
- ¹⁵ P. Baldi and K. Hornik, “Neural networks and principal component analysis: Learning from examples without local minima,” *Neural Netw.* **2**, 53–58 (1989).
- ¹⁶ G. Pérez-Hernández, F. Paul, T. Giorgino, G. De Fabritiis, and F. Noé, “Identification of slow molecular order parameters for Markov model construction,” *J. Chem. Phys.* **139**, 07B604_1 (2013).
- ¹⁷ R. R. Coifman, S. Lafon, A. B. Lee, M. Maggioni, B. Nadler, F. Warner, and S. W. Zucker, “Geometric diffusions as a tool for harmonic analysis and structure definition of data: Diffusion maps,” *Proc. Natl. Acad. Sci. U.S.A.* **102**, 7426–7431 (2005).
- ¹⁸ R. R. Coifman and S. Lafon, “Diffusion maps,” *Appl. Comput. Harmon. Anal.* **21**, 5–30 (2006).
- ¹⁹ B. Nadler, S. Lafon, R. R. Coifman, and I. G. Kevrekidis, “Diffusion maps, spectral clustering and reaction coordinates of dynamical systems,” *Appl. Comput. Harmon. Anal.* **21**, 113–127 (2006).
- ²⁰ R. R. Coifman, I. G. Kevrekidis, S. Lafon, M. Maggioni, and B. Nadler, “Diffusion maps, reduction coordinates, and low dimensional representation of stochastic systems,” *Multiscale Model. Simul.* **7**, 842–864 (2008).
- ²¹ G. E. Hinton and S. T. Roweis, “Stochastic neighbor embedding,” *NeurIPS* **15**, 833–864 (2002).
- ²² L. van der Maaten and G. Hinton, “Visualizing data using t-SNE,” *J. Mach. Learn. Res.* **9**, 2579–2605 (2008).
- ²³ L. van der Maaten, “Learning a parametric embedding by preserving local structure,” *J. Mach. Learn. Res.* **5**, 384–391 (2009).
- ²⁴ M. Ceriotti, G. A. Tribello, and M. Parrinello, “Simplifying the representation of complex free-energy landscapes using sketch-map,” *Proc. Natl. Acad. Sci. U.S.A.* **108**, 13023–13028 (2011).
- ²⁵ L. McInnes, J. Healy, and J. Melville, “UMAP: Uniform manifold approximation and projection for dimension reduction,” *arXiv preprint arXiv:1802.03426* (2018).
- ²⁶ S. T. Roweis and L. K. Saul, “Nonlinear dimensionality reduction by locally linear embedding,” *Science* **290**, 2323–2326 (2000).
- ²⁷ J. B. Tenenbaum, V. De Silva, and J. C. Langford, “A global geometric framework for nonlinear dimensionality reduction,” *Science* **290**, 2319–2323 (2000).
- ²⁸ W. Chen and A. L. Ferguson, “Molecular enhanced sampling with autoencoders: On-the-fly collective variable discovery and accelerated free energy landscape exploration,” *J. Comp. Chem.* **39**, 2079 (2018).
- ²⁹ C. X. Hernández, H. K. Wayment-Steele, M. M. Sultan, B. E. Husic, and V. S. Pande, “Variational encoding of complex dynamics,” *Phys. Rev. E* **97**, 062412 (2018).
- ³⁰ J. M. L. Ribeiro, P. Bravo, Y. Wang, and P. Tiwary, “Reweighted autoencoded variational Bayes for enhanced

- sampling (RAVE),” *J. Chem. Phys.* **149**, 072301 (2018).
- 31 W. Chen, A. R. Tan, and A. L. Ferguson, “Collective variable discovery and enhanced sampling using autoencoders: Innovations in network architecture and error function design,” *J. Chem. Phys.* **149**, 072312 (2018).
 - 32 C. Wehmeyer and F. Noé, “Time-lagged autoencoders: Deep learning of slow collective variables for molecular kinetics,” *J. Chem. Phys.* **148**, 241703 (2018).
 - 33 W. Chen, H. Sidky, and A. L. Ferguson, “Capabilities and limitations of time-lagged autoencoders for slow mode discovery in dynamical systems,” *J. Chem. Phys.* **151**, 064123 (2019).
 - 34 Y. B. Varolgunes, T. Bereau, and J. F. Rudzinski, “Interpretable embeddings from molecular simulations using Gaussian mixture variational autoencoders,” *Mach. Learn.: Sci. Technol.* **1**, 015012 (2020).
 - 35 A. Mardt, L. Pasquali, H. Wu, and F. Noé, “VAMPnets for deep learning of molecular kinetics,” *Nat. Commun.* **9**, 1 (2018).
 - 36 H. Wu and F. Noé, “Variational approach for learning Markov processes from time series data,” *J. Nonlinear Sci.* **30**, 23–66 (2020).
 - 37 H. Wu, A. Mardt, L. Pasquali, and F. Noé, “Deep generative Markov state models,” *NeurIPS* **31**, 3975–3984 (2018).
 - 38 M. Schöberl, N. Zabaras, and P.-S. Koutsourelakis, “Predictive collective variable discovery with deep Bayesian models,” *J. Chem. Phys.* **150**, 024109 (2019).
 - 39 M. Schöberl, N. Zabaras, and P.-S. Koutsourelakis, “Embedded-physics machine learning for coarse-graining and collective variable discovery without data,” *arXiv preprint arXiv:2002.10148* (2020).
 - 40 F. Noé, S. Olsson, J. Köhler, and H. Wu, “Boltzmann generators: Sampling equilibrium states of many-body systems with deep learning,” *Science* **365**, eaaw1147 (2019).
 - 41 S.-H. Li, C.-X. Dong, L. Zhang, and L. Wang, “Neural canonical transformation with symplectic flows,” *Phys. Rev. X* **10**, 021020 (2020).
 - 42 L. Bonati, V. Rizzi, and M. Parrinello, “Data-driven collective variables for enhanced sampling,” *J. Phys. Chem. Lett.* **11**, 2998–3004 (2020).
 - 43 J. Zhang and M. Chen, “Unfolding hidden barriers by active enhanced sampling,” *Phys. Rev. Lett.* **121**, 010601 (2018).
 - 44 L. van Der Maaten, “Accelerating t-SNE using tree-based algorithms,” *J. Mach. Learn. Res.* **15**, 3221–3245 (2014).
 - 45 S. Pant, Z. Smith, Y. Wang, E. Tajkhorshid, and P. Tiwary, “A statistical physics based approach to capture spurious solutions in AI-enhanced molecular dynamics,” *bioRxiv* (2020), <https://doi.org/10.1101/2020.06.11.146985>.
 - 46 G. M. Torrie and J. P. Valleau, “Nonphysical sampling distributions in Monte Carlo free-energy estimation: Umbrella sampling,” *J. Comp. Phys.* **23**, 187–199 (1977).
 - 47 T. Huber, A. E. Torda, and W. F. Gunsteren, “Local elevation: A method for improving the searching properties of molecular dynamics simulation,” *J. Computer-Aided Mol. Des.* **8**, 695–708 (1994).
 - 48 E. Darve and A. Pohorille, “Calculating free energies using average force,” *J. Chem. Phys.* **115**, 9169 (2001).
 - 49 F. Wang and D. Landau, “Efficient, multiple-range random walk algorithm to calculate the density of states,” *Phys. Rev. Lett.* **86**, 2050–2053 (2001).
 - 50 U. Hansmann and L. Wille, “Global optimization by energy landscape paving,” *Phys. Rev. Lett.* **88**, 068105 (2002).
 - 51 P. Maragakis, A. van der Vaart, and M. Karplus, “Gaussian-mixture umbrella sampling,” *J. Phys. Chem. B* **113**, 4664–4673 (2009).
 - 52 A. Laio and M. Parrinello, “Escaping free-energy minima,” *Proc. Natl. Acad. Sci. U.S.A.* **99**, 12562–12566 (2002).
 - 53 A. Barducci, G. Bussi, and M. Parrinello, “Well-tempered metadynamics: A smoothly converging and tunable free-energy method,” *Phys. Rev. Lett.* **100**, 020603 (2008).
 - 54 O. Valsson and M. Parrinello, “Variational approach to enhanced sampling and free energy calculations,” *Phys. Rev. Lett.* **113**, 090601 (2014).
 - 55 O. Valsson and M. Parrinello, “Variationally enhanced sampling,” in *Handbook of Materials Modeling: Methods: Theory and M* edited by W. Andreoni and S. Yip (Springer International Publishing, Cham, 2020) pp. 621–634.
 - 56 M. Invernizzi and M. Parrinello, “Rethinking metadynamics: From bias potentials to probability distributions,” *J. Phys. Chem. Lett.* **11**, 2731–2736 (2020).
 - 57 P. Tiwary and M. Parrinello, “A time-independent free energy estimator for metadynamics,” *J. Phys. Chem. B* **119**, 736–742 (2015), <http://dx.doi.org/10.1021/jp504920s>.
 - 58 M. Bonomi, A. Barducci, and M. Parrinello, “Reconstructing the equilibrium Boltzmann distribution from well-tempered metadynamics,” *J. Comp. Chem.* **30**, 1615–1621 (2009).
 - 59 D. Branduardi, G. Bussi, and M. Parrinello, “Metadynamics with adaptive gaussians,” *J. Chem. Theory Comput.* **8**, 2247–2254 (2012).
 - 60 F. Giberti, B. Cheng, G. A. Tribello, and M. Ceriotti, “Iterative unbiasing of quasi-equilibrium sampling,” *J. Chem. Theory Comput.* **16**, 100–107 (2019).
 - 61 T. M. Schäfer and G. Settanni, “Data reweighting in metadynamics simulations,” *J. Chem. Theory Comput.* **16**,

- 2042–2052 (2020).
- 62 The PLUMED Consortium, “Promoting transparency and reproducibility in enhanced molecular simulations,” *Nat. Methods* **16**, 670–673 (2019), For the full list of researches from the PLUMED Consortium, see <https://www.plumed-nest.org/consortium.html>.
 - 63 J. Rydzewski and W. Nowak, “Machine learning based dimensionality reduction facilitates ligand diffusion paths assessment: A case of cytochrome P450cam,” *J. Chem. Theory Comput.* **12**, 2110–2120 (2016).
 - 64 H. Zhou, F. Wang, and P. Tao, “t-distributed stochastic neighbor embedding method with the least information loss for macromolecular simulations,” *J. Chem. Theory Comput.* **14**, 5499–5510 (2018).
 - 65 V. Spiwok and P. Kříž, “Time-lagged t-distributed stochastic neighbor embedding (t-SNE) of molecular simulation trajectories,” *arXiv preprint arXiv:2003.02505* (2020).
 - 66 O. Fleetwood, J. Carlsson, and L. Delemotte, “Identification of ligand-specific g-protein coupled receptor states and prediction of downstream efficacy via data-driven modeling,” *bioRxiv* (2020), 10.1101/2020.07.06.186601, <https://www.biorxiv.org/content/early/2020/07/06/2020.07.06.186601.full.pdf>.
 - 67 A. Caticha, “Relative entropy and inductive inference,” *AIP Conf. Proc.* (2004), 10.1063/1.1751358.
 - 68 M. S. Shell, “The relative entropy is fundamental to multiscale and inverse thermodynamic problems,” *J. Chem. Phys.* **129**, 144108 (2008).
 - 69 Z. Rached, F. Alajaji, and L. L. Campbell, “The Kullback-Leibler divergence rate between Markov sources,” *IEEE Trans. Inf. Theory* **50**, 917 (2004).
 - 70 T. Hofmann, B. Schölkopf, and A. J. Smola, “Kernel methods in machine learning,” *Ann. Stat.* **36**, 1171–1220 (2008).
 - 71 J. M. Lee, “Introduction to smooth manifolds,” (Springer-Verlag New York, 2003).
 - 72 A. Globerson, G. Chechik, F. Pereira, and N. Tishby, “Euclidean embedding of co-occurrence data,” *J. Mach. Learn. Res.* **8**, 2265–2295 (2007).
 - 73 W. Zheng, A. V. Vargiu, M. A. Rohrdanz, P. Carloni, and C. Clementi, “Molecular recognition of DNA by ligands: Roughness and complexity of the free energy profile,” *J. Chem. Phys.* **139**, 10B612_1 (2013).
 - 74 J. Preto and C. Clementi, “Fast recovery of free energy landscapes via diffusion-map-directed molecular dynamics,” *Phys. Chem. Chem. Phys.* **16**, 19181 (2014).
 - 75 T. M. Cover and J. A. Thomas, *Elements of information theory*, 2nd ed. (John Wiley & Sons, 2006).
 - 76 M. Wattenberg, F. Viégas, and I. Johnson, “How to use t-SNE effectively,” *Distill* (2016), 10.23915/distill.00002.
 - 77 J. A. Lee, D. H. Peluffo-Ordóñez, and M. Verleysen, “Multiscale stochastic neighbor embedding: Towards parameter-free dimensionality reduction,” in *ESANN* (2014).
 - 78 J. W. Sammon, “A nonlinear mapping for data structure analysis,” *IEEE Trans. Comput.* **100**, 401–409 (1969).
 - 79 Y. LeCun, Y. Bengio, and G. Hinton, “Deep learning,” *Nature* **521**, 436 (2015).
 - 80 D. P. Kingma and J. Ba, “Adam: A method for stochastic optimization,” *ICLR* **3** (2015), 1412.6980v9.
 - 81 I. Guyon and A. Elisseeff, “An introduction to variable and feature selection,” *J. Mach. Learn. Res.* **3**, 1157–1182 (2003).
 - 82 G. James, D. Witten, T. Hastie, and R. Tibshirani, *An introduction to statistical learning*, 8th ed. (Springer, 2017).
 - 83 G. A. Tribello and P. Gasparotto, “Using dimensionality reduction to analyze protein trajectories,” *Front. Mol. Biosci.* **6**, 46 (2019).
 - 84 G. A. Tribello and P. Gasparotto, “Using data-reduction techniques to analyze biomolecular trajectories,” in *Biomolecular Simulations: Methods and protocols* (Springer, 2019) p. 453.
 - 85 D. S. Hochbaum and D. B. Shmoys, “A best possible heuristic for the k-center problem,” *Math. Oper. Res.* **10**, 180–184 (1985).
 - 86 M. Ceriotti, G. A. Tribello, and M. Parrinello, “Demonstrating the transferability and the descriptive power of sketch-map,” *J. Chem. Theory Comput.* **9**, 1521–1532 (2013).
 - 87 A. Paszke, S. Gross, F. Massa, A. Lerer, J. Bradbury, G. Chanan, T. Killeen, Z. Lin, N. Gimelshein, L. Antiga, A. Desmaison, A. Kopf, E. Yang, Z. DeVito, M. Raison, A. Tejani, S. Chilamkurthy, B. Steiner, L. Fang, J. Bai, and S. Chintala, “PyTorch: An imperative style, high-performance deep learning library,” *NeurIPS* **33**, 8024–8035 (2019).
 - 88 A. Paszke, S. Gross, S. Chintala, G. Chanan, E. Yang, Z. DeVito, Z. Lin, A. Desmaison, L. Antiga, and A. Lerer, “Automatic differentiation in PyTorch,” *NeurIPS* **31** (2017).
 - 89 K. Müller and L. D. Brown, “Location of saddle points and minimum energy paths by a constrained simplex optimization procedure,” *Theor. Chim. Acta.* **53**, 75–93 (1979).
 - 90 G. Bussi and M. Parrinello, “Accurate sampling using Langevin dynamics,” *Phys. Rev. E* **75**, 056707 (2007).
 - 91 M. J. Abraham, T. Murtola, R. Schulz, S. Páll, J. C. Smith, B. Hess, and E. Lindahl, “GROMACS: High performance molecular simulations through multi-level parallelism from laptops to supercomputers,” *SoftwareX* **1–2**, 19–25 (2015).

- ⁹² V. Hornak, R. Abel, A. Okur, B. Strockbine, A. Roitberg, and C. Simmerling, “Comparison of multiple Amber force fields and development of improved protein backbone parameters,” *Proteins* **65**, 712–725 (2006).
- ⁹³ G. Bussi, D. Donadio, and M. Parrinello, “Canonical sampling through velocity rescaling,” *J. Chem. Phys.* **126**, 014101 (2007).
- ⁹⁴ B. Hess, “P-LINCS: A parallel linear constraint solver for molecular simulation,” *J. Chem. Theory Comput.* **4**, 116–122 (2008).
- ⁹⁵ G. E. Hinton and R. R. Salakhutdinow, “Reducing the dimensionality of data with neural networks,” *Science* **313**, 504–507 (2006).
- ⁹⁶ A. L. Maas, A. Y. Hannun, and A. Y. Ng, “Rectifier nonlinearities improve neural network acoustic models,” *J. Mach. Learn. Res.* **28**, 1 (2013).
- ⁹⁷ N. Srivastava, G. Hinton, A. Krizhevsky, I. Sutskever, and R. Salakhutdinov, “Dropout: A simple way to prevent neural networks from overfitting,” *J. Mach. Learn. Res.* **15**, 1929–1958 (2014).
- ⁹⁸ X. Glorot and Y. Bengio, “Understanding the difficulty of training deep feedforward neural networks,” *J. Mach. Learn. Res.* **9**, 249–256 (2010).
- ⁹⁹ C. M. Bishop, *Pattern recognition and machine learning* (Springer, 2006).
- ¹⁰⁰ F. Pedregosa, G. Varoquaux, A. Gramfort, V. Michel, B. Thirion, O. Grisel, M. Blondel, P. Prettenhofer, R. Weiss, V. Dubourg, J. Vanderplas, A. Passos, D. Cournapeau, M. Brucher, M. Perrot, and E. Duchesnay, “scikit-learn: Machine learning in Python,” *J. Mach. Learn. Res.* **12**, 2825–2830 (2011).
- ¹⁰¹ P. Virtanen, R. Gommers, T. E. Oliphant, M. Haberland, T. Reddy, D. Cournapeau, E. Burovski, P. Peterson, W. Weckesser, J. Bright, S. J. van der Walt, M. Brett, J. Wilson, K. Jarrod Millman, N. Mayorov, A. R. J. Nelson, E. Jones, R. Kern, E. Larson, C. J. Carey, Í. Polat, Y. Feng, E. W. Moore, J. VanderPlas, D. Laxalde, J. Perktold, R. Cimrman, I. Henriksen, E. A. Quintero, C. R. Harris, A. M. Archibald, A. H. Ribeiro, F. Pedregosa, P. van Mulbregt, and S. . . Contributors, “SciPy 1.0: Fundamental algorithms for scientific computing in Python,” *Nat. Methods* **17**, 261–272 (2020).
- ¹⁰² R. H. Swendsen and J.-S. Wang, “Replica Monte Carlo simulation of spin-glasses,” *Phys. Rev. Lett.* **57**, 2607 (1986).
- ¹⁰³ O. Kukharenko, K. Sawade, J. Steuer, and C. Peter, “Using dimensionality reduction to systematically expand conformational sampling of intrinsically disordered peptides,” *J. Chem. Theory Comput.* **12**, 4726–4734 (2016).
- ¹⁰⁴ S. Hunkler, T. Lemke, C. Peter, and O. Kukharenko, “Back-mapping based sampling: Coarse grained free energy landscapes as a guideline for atomistic exploration,” *J. Chem. Phys.* **151**, 154102 (2019).